Matter and Radiation at Extremes

RESEARCH ARTICLE | AUGUST 16 2024

Equation of state for boron nitride along the principal Hugoniot to 16 Mbar

Huan Zhang ; Yutong Yang ; Weimin Yang; Zanyang Guan ; Xiaoxi Duan ; Mengsheng Yang ; Yonggang Liu; Jingxiang Shen; Katarzyna Batani ; Diluka Singappuli; Ke Lan ; Yongsheng Li ; Wenyi Huo ; Hao Liu; Yulong Li; Dong Yang; Sanwei Li; Zhebin Wang ; Jiamin Yang ; Zongqing Zhao; Weiyan Zhang; Liang Sun ; Wei Kang ; Dimitri Batani

Check for updates

Matter Radiat. Extremes 9, 057403 (2024)
https://doi.org/10.1063/5.0206889

View Online
Export Citation

23 September 2024 06:07:34

AIP Publishing

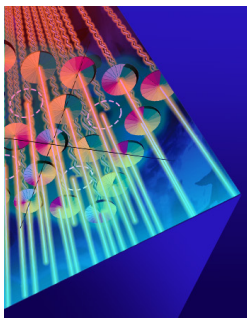

Matter and Radiation at Extremes

Special Topics Now Online

Read Now

AIP Publishing

Matter and Radiation at Extremes

RESEARCH ARTICLE

pubs.aip.org/aip/mre

Featured

Equation of state for boron nitride along the principal Hugoniot to 16 Mbar

Cite as: Matter Radiat. Extremes 9, 057403 (2024); doi: 10.1063/5.0206889
Submitted: 4 March 2024 • Accepted: 12 June 2024 •
Published Online: 16 August 2024

View Online Export Citation CrossMark

Huan Zhang,[1] Yutong Yang,[2,3] Weimin Yang,[1] Zanyang Guan,[1] Xiaoxi Duan,[1] Mengsheng Yang,[1] Yonggang Liu,[1] Jingxiang Shen,[3] Katarzyna Batani,[4] Diluka Singappuli,[5] Ke Lan,[6] Yongsheng Li,[6] Wenyi Huo,[6] Hao Liu,[1,6] Yulong Li,[1] Dong Yang,[1] Sanwei Li,[1] Zhebin Wang,[1] Jiamin Yang,[1] Zongqing Zhao,[1] Weiyan Zhang,[3] Liang Sun,[1,a)] Wei Kang,[3,a)] and Dimitri Batani[5,a)]

AFFILIATIONS

[1] National Key Laboratory of Plasma Physics, Laser Fusion Research Center, China Academy of Engineering Physics, Mianyang 621900, China
[2] HEDPS, Center for Applied Physics and Technology, and College of Physics, Peking University, Beijing 100871, China
[3] HEDPS, Center for Applied Physics and Technology, and School of Engineering, Peking University, Beijing 100871, China
[4] Institute of Plasma Physics and Laser Microfusion, Hery 23, 01-497 Warszawa, Poland
[5] Université de Bordeaux, CNRS, CEA, CELIA (Centre Lasers Intenses et Applications), UMR 5107, F-33405 Talence, France
[6] Institute of Applied Physics and Computational Mathematics, Beijing 100094, China

[a)] **Authors to whom correspondence should be addressed:** sunliangyp@outlook.com; weikang@pku.edu.cn; and dimitri.batani@u-bordeaux.fr

ABSTRACT

The thermodynamic properties of boron nitride under extreme pressures and temperatures are of great interest and importance for materials science and inertial confinement fusion physics, but they are poorly understood owing to the challenges of performing experiments and realizing *ab initio* calculations. Here, we report the first shock Hugoniot data on hexagonal boron nitride at pressures of 5–16 Mbar, using hohlraum-driven shock waves at the SGIII-p laser facility in China. Our density functional theory molecular dynamics calculations closely match experimental data, validating the equations of state for modeling the shock response of boron nitride and filling a crucial gap in the knowledge of boron nitride properties in the region of multi-Mbar pressures and eV temperatures. The results presented here provide fundamental insights into boron nitride under the extreme conditions relevant to inertial confinement fusion, hydrogen–boron fusion, and high-energy-density physics.

© 2024 Author(s). All article content, except where otherwise noted, is licensed under a Creative Commons Attribution (CC BY) license (https://creativecommons.org/licenses/by/4.0/). https://doi.org/10.1063/5.0206889

I. INTRODUCTION

Understanding the behavior of boron and its compounds under extreme conditions of high pressure and temperature is important in a number of scientific fields. This behavior plays a fundamental role in the "boron dip" phenomenon,[1–3] which is of key importance in stellar nucleosynthesis and other areas of nuclear astrophysics, and its investigation has motivated a number of laboratory experiments.[4,5] In addition to this, interest in boron and its compounds has recently grown rapidly for a variety of other reasons. Among these is the possibility of hydrogen–boron (HB) fusion, which has the very desirable characteristic of not producing neutrons, unlike the deuterium–tritium (DT) reaction. Unfortunately, to trigger this reaction in a laboratory plasma, a very high temperature is required, which explains why most fusion research has focused on DT, leaving HB fusion as a remote, although interesting, "second step" in energy production through fusion. However, very recent experiments, using both laser-driven[6] and magnetic-confinement approaches,[7,8] have reawakened interest in HB fusion, which is currently a very active research field.

Boron compounds are also of great interest in the context of investigations of materials under high-energy-density conditions. In

23 September 2024 06:07:34

particular, boron nitride (BN) is in many respects similar to carbon. Its two main allotropic phases, hexagonal boron nitride (h-BN) and cubic boron nitride (c-BN), with different initial densities, are similar in structure and mass density to graphite and diamond, respectively. The average atomic and mass numbers (Z and A) of BN are the same as those of carbon. The phase diagram for BN remains experimentally unverified at high pressure, with potential differences from that of carbon, arising from the fact that BN is composed of two elements. Obtaining an understanding the BN phase diagram is an important test of theoretical models of the equation of state of matter (EoS) under extreme conditions.[9–11] For this reason, the EoS and the phase transitions of BN have been extensively studied up to pressures of a couple of Mbar (1 Mbar = 100 GPa) using static compression methods (diamond anvil cells).[12–14] Some data can also be found in the RUSBANK.[15,16]

Finally, pure boron and boron compounds are interesting in the context of inertial confinement fusion (ICF),[17–19] because they have been proposed as ablators for implosion experiments as an alternative to synthetic diamond (HDC). The nuclear reactions of boron and nitrogen with neutrons, protons, and γ rays offer the potential for additional diagnostic channels to better constrain the shell areal density and ablator mixing during nuclear burn time.[20,21] However, the main interest in BN with regard to ICF arises from the fact that the melting temperature and bulk modulus of diamond are very high. Thus, the initial foot in the laser pulse temporal profile used to drive implosion cannot be too low, implying that the shock pressure generated by the initial foot in current experiments is of the order of 10 Mbar, which sets a quite high value of the entropy parameter. Therefore, while diamond has been a key factor in demonstrating fusion breakthrough at the National Ignition Facility (NIF),[22] its use can be problematic when attempts are made to achieve high-gain implosions. Hence, the search for alternative ablator materials is important, and, in this respect, BN could be of interest because of its lower melting temperature and bulk modulus.

Despite all these reasons to study the EoS of boron compounds at very high pressure, the available experimental data at pressures greater than 1 Mbar are very scarce. At the OMEGA laser facility, Shuai Zhang and co-workers have obtained only three EoS data of c-BN along the principal Hugoniot above 12 Mbar using the direct-drive approach and transparent monocrystalline samples.[23] At the NIF, the same group has measured one experimental point on the shock Hugoniot for pure boron at very high pressure (>56 Mbar) using an indirect-drive.[24] The result agreed with a first-principles EoS model that predicts a maximum compression of 4.6, slightly larger than those predicted by the Thomas–Fermi models LEOS 50 and SESAME 2330. Finally, measurements of the EoS of boron carbide (B_4C) have been made both at OMEGA[25] and at the NIF.[26] At OMEGA, indirectly driven shocks were produced using a half-hohlraum. At NIF, seven experimental points were obtained at pressures between 29 and 61 Mbar. Data were compared with theoretical models, demonstrating good agreement with an average-atom model (LEOS 2122).[27] Thus, only a few experimental data at high pressure and temperature have been obtained, and they are too limited to constrain theoretical models above a few megabar. In addition, the properties of boron compounds under extreme conditions should be significantly influenced by their varying initial densities.

In this context, we performed an experiment on the SGIII prototype (SGIII-p) laser facility in China[28] to study the EoS of BN along the Hugoniot curve with the goals of increasing the available dataset and providing further validation of theoretical models. Also, since the Hugoniots of BN with different initial phases can show significant differences, we used h-BN samples in our experiment. Therefore, our data extend and complement those obtained at OMEGA using c-BN. Our results cover the pressure range between 5 and 16 Mbar, corresponding to a near-threefold compression of h-BN. They also can contribute to understanding the structural complexity in the phase diagram of BN and how the phase changes upon compression. For this reason, in parallel to the experiments, we carried out density functional theory molecular dynamics (DFT-MD) calculations for h-BN, with the results showing good agreement with experimental data. This provides better confidence in model predictions of the physical properties of BN, thereby allowing us to draw conclusions regarding the adaptability of BN as an ablator for ICF experiments, and to assess the efficiency of BN as a boron supplier in HB fusion experiments.

II. LASER SHOCK EXPERIMENT

A laser shock compression experiment for h-BN was conducted at the SGIII-p laser facility,[28,29] located at the Laser Fusion Research Center (LFRC) in Mianyang, China. The system operates with a Nd:glass laser at a wavelength of 351 nm through frequency-tripling. Eight laser beams were smoothed by distributed phase plates, producing a focus spot of 500 μm diameter. They deliver a flat-top laser (UV, 351 nm) pulse with a duration of 2–4 ns and an energy up to 6400 J into the entrance holes of a cylindrical gold hohlraum. A multilayer step-target package was attached to the side, as depicted in Fig. 1. The uniform intense radiation field created inside the hohlraum irradiated the Al pusher of the target package, leading to the generation of a strong shock wave that propagated through both the BN sample and the reference materials. Time-resolved X-ray radiation temperatures were measured by flat-response X-ray diodes (FXRDs).[30,31] Two types of hohlraum were used in this experiment to cover a broader shock pressure range. The details of the hohlraum and samples are given in the supplementary material.

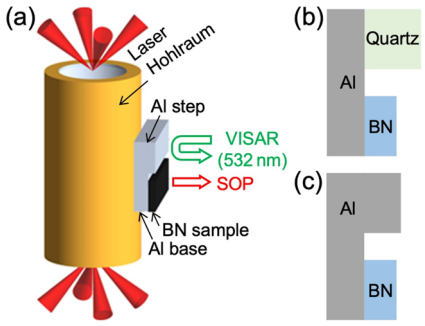

FIG. 1. (a) Schematic of experimental configuration. The planar sample package is attached to the side of the hohlraum. Two types of sample packages were used. (b) The first type consists of an Al pusher plate, the BN sample, and the quartz standard to measure the *in situ* shock velocity profile. (c) The second type uses an Al step instead of the quartz standard.

23 September 2024 06:07:34

© Author(s) 2024

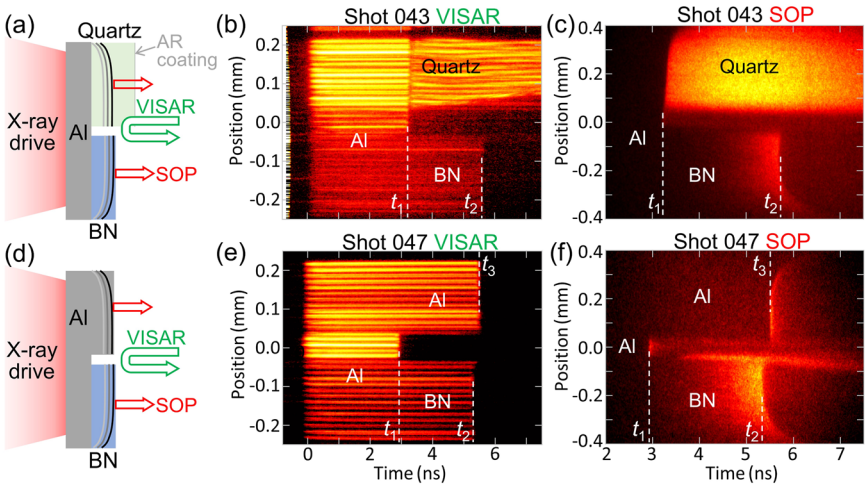

FIG. 2. Experimental configurations and typical data from the shots. The surface reflection and thermal emission signals were recorded by VISAR and SOP, for the Al base, BN sample, and quartz/Al-step standards. (a) Schematic of Al–BN–quartz-type EoS target. (b) Time-resolved VISAR and (c) SOP data for shot 043 using this type of target. t_1 marks the time when the shock crosses the interface between Al and BN, and t_2 marks the shock breakout time from the rear surface of the BN sample. After t_1, the shock propagates in the transparent quartz standard, with its shock front being monitored by VISAR. (d) Schematic of the Al–BN–Al-type target. (e) VISAR and (f) SOP data for shot 047. Three times are measured: t_1 is the time when the shock enters the BN sample, and t_2 and t_3 are the shock breakout times from the BN sample and the Al step, respectively. Since the our BN sample is porous, gradually increasing thermal emission ahead of shock breakout can be observed for BN, as shown in (c) and (f).

Hexagonal BN samples compressed from high purity h-BN powder were used in the present experiment. The BN samples with initial density 2.04–2.05 g/cm^3 were provided by the LFRC target group and by the company Scitech Precison, UK. As shown in Fig. 1, two types of samples were used to obtain shock Hugoniot EoS data by the impedance matching (IM) technique.[32–34] The first type consisted of an Al base (pusher) and two samples of Al (reference material) and BN, in the shape of steps (Al–BN–Al). The second type was Al–BN–quartz, which provided a detailed history of the shock velocity in the quartz (and hence indirectly in the BN). A thin Al film (of the order of 100 nm) was coated on the rear surface of the BN sample to provide a reflecting signal for the line velocity interferometer system for any reflector (VISAR) diagnostic.[35]

The primary ultrafast diagnostics used in the experiment were the VISAR, with a 532 nm probe laser, and a streaked optical pyrometer (SOP) system,[36–38] which measured time-resolved thermal emission. Figure 2 shows the signals from the Al–BN–quartz and Al–BN–Al samples recorded by VISAR and SOP. The shock breakout times from the Al base and the BN sample were recorded simultaneously. As quartz becomes reflective above 1.5 Mbar,[39] the fringe shift in the VISAR images provides a one-dimensional history of the shock velocity in the quartz.

The initial densities were 2.65 g/cm^3 for quartz and 2.70 g/cm^3 for Al (reference material). The refractive index of quartz at 532 nm is 1.547. In this experiment, we used two VISAR channels with different velocity sensitivities. Their respective etalons were 5.007 and 6.972 mm thick, corresponding to respective velocity sensitivities of 6.433 and 4.620 km/s per fringe in the quartz. To analyze the VISAR images, we used the Fourier transform method proposed in Ref. 35, which provides the phase shifts resulting from changes in velocity. The uncertainty in determining the phase was estimated as 5% of a fringe, which resulted in an uncertainty of ~1% for shock velocities. The VISAR system used two streak cameras with 10 ns sweep duration, resulting in temporal sensitivities of ~20 ps.

III. THEORETICAL DFT-MD RESULTS

The Hugoniot of h-BN can be obtained from the EoS data calculated using the DFT-MD method.[40,41] The principal Hugoniot is calculated through the Rankine–Hugoniot relation:

$$E_1 - E_0 = \frac{1}{2}(V_0 - V_1)(P_0 + P_1) \quad (1)$$

where subscript 1 indicates the shock-compressed state and 0 the initial state, E is the internal energy per formula unit of BN, and V is the volume per formula unit. The choice of E_0 is a subtle issue in calculations for porous materials. In the experiments, the initial temperature and density were T_0 = 300 K and ρ_0 = 2.04–2.05 g/cm^3, respectively. Usually, one might expect that the energy and pressure under this condition could be directly calculated with the DFT-MD method by solving the Kohn–Sham equation. However, for porous materials, the ionic configuration is generally unknown because the materials are usually amorphous with irregular pore distribution and complex nonperiodic internal structure, which result in significantly different response behaviors compared with homogeneous materials. Accurately assessing the internal energy per formula unit can therefore be challenging.

In Fig. 3(a), we show the Hugoniots of BN for selected values of E_0. The curve begins in the cubic phase at low compression ratio, and, with further compression, it enters the fluid region. While the Hugoniot curve is not very sensitive to the initial pressure P_0 (since the generally $P_1 \gg P_0$), it is sensitive to the initial-state internal energy E_0, as shown in Fig. 3(a). We have chosen the value of E_0 = −38.44 Ry that best fits the experimental data of RUSBANK

23 September 2024 06:07:34

© Author(s) 2024

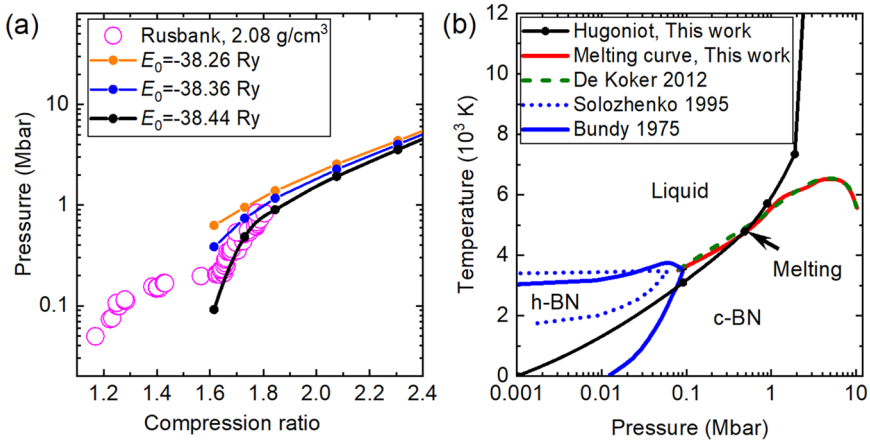

FIG. 3. Theoretical calculations of BN EoS at high pressures using the DFT-MD method, compared with previous results. (a) Principal Hugoniot calculated with three different choices of initial energy density E_0 with initial density 2.08 g/cm^3. The Hugoniot with E_0 = −38.44 Ry/formula-unit best matches the previous experimental results (empty circles). (b) BN phase diagram in the pressure range relevant to this study. The best-match Hugoniot crosses the solid–liquid boundary at ~1 Mbar pressure. The melting curve for c-BN (solid red) agrees well with the previous theoretical result (dashed green).

(ρ_0 = 2.08 g/cm^3 and T_0 = 300 K)[16] at low pressure as the initial-state internal energy (which is much higher than the E_0 for pure h-BN of −38.59 Ry and pure c-BN of −38.60 Ry), and it reproduces the experimental data under high pressure well.

Moreover, BN is assumed in the cubic phase to reproduce the RUSBANK experimental data before melting, implying that the porous h-BN sample undergoes a phase transition to the cubic phase before it melts. This phase transition along the Hugoniot is also well illustrated in the phase diagram displayed in Fig. 3(b). The blue dotted and solid lines in Fig. 3(b) represent the phase diagrams of BN measured in previous experiments. Here, we adopt the same method as de Koker[42] to calculate the melting curve between the cubic solid phase and liquid phase of BN. The melting curve starts from the triple point of the cubic–hexagonal–liquid phases of BN. The temperature $T_{\rm tri}$ = 3472.0 K and pressure $P_{\rm tri}$ = 0.069 42 Mbar of the triple point are determined as the averages of the measurements of Corrigan and Bundy[43] and those of Solozhenko.[44] The melting temperature T_M at higher pressure is then determined by integrating the Clapeyron equation

$$\frac{dT}{dP} = \frac{\Delta V}{\Delta S} \tag{2}$$

for the slope of the melting curve, where ΔV is the volume change between the two phases and ΔS is the change in entropy. In the DFT-MD calculation, we first calculate the internal energy E and volume V of BN in both liquid and cubic solid phases at the pressure and temperature of a known state point on the melting curve, such as the triple point. ΔV is calculated as the volume difference of the two phases, and ΔS is calculated through the energy difference ΔE together with ΔV via $\Delta S = (\Delta E + P\Delta V)/T$. The next point on the melting curve can then be calculated by integrating Eq. (2) with a small step in ΔP. When this procedure is repeated, the entire melting curve between the c-BN and liquid phases can be obtained.

Figure 3(b) displays the calculated Hugoniot curve and the equilibrium melting curve together with phase boundaries between h-BN and c-BN from previous experiments. It can be seen that the porous h-BN is compressed into the cubic phase at ~0.1 Mbar, and melts along the cubic–liquid phase boundary at a pressure ~1 Mbar. This shows that the melting temperature of h-BN along the principal Hugoniot is ~4800 K. Note that the equilibrium phase boundaries calculated thermodynamically are usually lower than the boundaries deduced from experimental Hugoniot data without considering the dynamical effects associated with overcoming the energy barriers in phase transitions under dynamical shock compression.

All the DFT-MD calculations are performed using the Quantum ESPRESSO package.[45] The local-density-approximation (LDA)[46] version of the exchange-correlation functional is used, and pseudopotentials for boron and nitrogen elements are generated using the ATOMPAW program[47] in a projected-augmented-wave (PAW) form.[48] The core cutoff radii for both elements are 1.4 Bohr, with all electrons in the L shell treated as active electrons, and the cutoff for plane-wave energy in the calculation is 140 Ry. The EoS data are calculated with 216 atoms in a simulation box. The Brillouin zone is sampled with the Γ point.

We follow the routines described in previous works[49–54] to calculate EoS tables and Hugoniots. The EoS calculations are performed in canonical ensembles (NVT ensembles), where the ion temperatures are controlled by the velocity-rescaling technique. Electrons follow the Fermi–Dirac distribution at the given T. The time step is 0.4–0.8 fs, which is less than the duration that it takes for an ion to traverse the average interatomic distance at its thermal velocity divided by a factor of l, which in this work is set to be 60, i.e.,

$$dt = \frac{1}{l}\frac{\left(\frac{3}{4\pi n}\right)^{1/3}}{\left(\frac{T}{m}\right)^{1/2}}, \tag{3}$$

where n is the number density, and m is the average mass of B and N atoms. The results of the EoS are then obtained statistically by averaging thermodynamic quantities over 1000–1500 steps following the attainment of MD equilibrium after 3000 steps. For solid h-BN and

23 September 2024 06:07:34

© Author(s) 2024

c-BN, both EoS are calculated with crystalline structures, while for the liquid state and above, the EoS is calculated from initially random ionic configurations. When computing the Rankine–Hugoniot curve, the Hugoniot equation is solved by varying the temperature while fixing the compression ratio. Extra calculations of EoS data around the Hugoniot points are performed in addition to the original EoS table to improve the temperature resolution to be smaller than 0.5 eV.

IV. ANALYSIS AND DISCUSSION

As illustrated in Fig. 2, we did not observe any fringe shift in VISAR from the Al base, and there is no obvious thermal emission recorded in SOP images before the shock breakout. This indicates that the preheating effect of X rays by indirect drive (heating the sample to a temperature lower than the melting temperature of Al) was negligible. Also, both VISAR and SOP images show that the produced shock front was spatially very flat (except at the very edges of the shock front, where some curvature was expected), and so the uncertainly due to shock nonplanarity can also be ignored in our experimental measurement.

In the case of Al–BN–quartz targets, as described in Figs. 2 and 4, the average shock velocity U_S^{BN} for the opaque h-BN was obtained from the thickness of the BN sample and the shock-wave transit time Δt_{BN}. In the transparent reference quartz, instead, the average shock velocity in quartz U_S^{Qz} was calculated as the average of the values measured by VISAR up to the same time Δt_{BN}. The two values U_S^{BN} and U_S^{Qz} were used as input data for calculation of the EoS data.

We applied the correction method for nonstationary shocks.[32–34,55] For the opaque BN sample, we considered the fluctuations of shock velocities to be similar to those of transparent quartz, if driven by the same radiation source.[25,34] Thus, the evolution history for shock velocity in opaque BN could be inferred from the shock velocity history in quartz. Then, the average shock velocity U_S^{BN} for the BN sample was corrected by introducing an inherent time modulation factor $F_{BN-quartz}$, which mainly depends on the EoS and sound speed of the materials. On the basis of our DFT-MD calculations for the EoS and sound speed of BN (the details of which are described in the supplementary material and the data are shown in Table S1 and S2), the modulation factor $F_{BN-quartz}$ was obtained to be ~0.99, and so this correction was also negligible. This was also expected, since the shock was quite stationary (see Fig. 4).

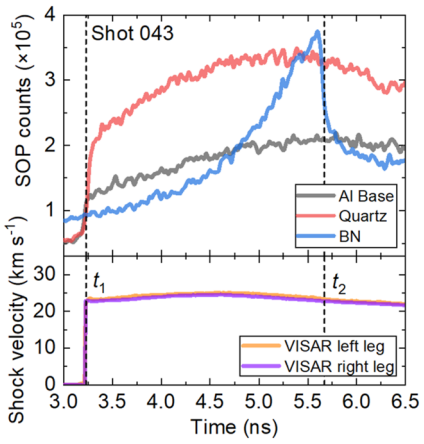

FIG. 4. Analysis of VISAR and SOP data for the Al–BN–quartz target in shot 043. The upper panel shows time-resolved SOP counts in the Al base, BN sample, and quartz standard. t_1 and t_2 are the shock breakout times from the rear surface of the Al base and BN sample, respectively. t_1 was determined as the half-height time of the rising edge of the SOP signals, while t_2 was determined as the half-height time of the corresponding dropping edge. The shock transit time through the BN sample is $\Delta t_{BN} = t_2 - t_1$. The lower panel shows the shock velocity profiles in the quartz standard, extracted from the two VISAR legs. The average quartz shock velocity calculated between t_1 and t_2 is used in the IM analysis.

The SOP images in Fig. 2 show that the thermal emission from the BN step was observed before shock breakout and was initially weak but then increased with time. This was probably due to the lower-than-nominal density of our h-BN samples, which implies that the material had some porosity. Therefore, the emission from the shock inside BN through the uncompressed material ahead of the shock front could be observed at certain distances. The signal then increased as the shock approached the rear surface, reducing the thickness of the uncompressed BN layer. After the shock breakout, the emission vanished, owing to the rapid expansion and cooling of the released material on the rear side of the target, as illustrated in Fig. 4. For the Al step, the usual behavior was observed, and no thermal emission appeared before shock breakout. In this case, the shock breakout time for Al was measured at the half-height of the rising slope in the SOP intensity history, and that for BN was measured at the half-height of the descending edge, as shown in Fig. 4.

The shock velocity in the Al base was calculated with the IM technique using the shock velocity in quartz combined with the EoS of quartz and Al. For the principal Hugoniot of Al, we used the piecewise-linear form of the $U_s - u_p$ relationship from Celliers *et al.* (Ref. 56), which gives $U_s = (17.992 \pm 0.078) + (1.167 \pm 0.026)(u_p - 9.838)$. For quartz, we used the analytical fit of the principal Hugoniot proposed by Hamel *et al.*[57] The piecewise formula is expressed as

$$U_S = \begin{cases} a + bU_p + cU_p^2 \; for \; U_p < U_{p1}, \\ (a - cU_{p1}^2) + bU_p + 2cU_pU_{p1} \; for \; U_p > U_{p1}, \end{cases}$$

where $a = 2.4(\pm 0.1)$ km/s, $b = 1.68(\pm 0.02)$, $c = -0.0155$ (± 0.001)km/s, and $U_{p1} = 15$ km/s. The shock compression state in BN can be obtained by IM analysis using the deduced shock velocity in the Al base and the measured average shock velocity in the BN. A graphical illustration of the IM analysis is shown in Fig. 5. The Al base is shocked to a high-pressure state along its principal Hugoniot, and the quartz and BN are shocked to relatively lower pressures along the release curve of Al when the shock crosses the interfaces between Al and these samples. The state of the compressed quartz is determined by the crossing point of the Hugoniot for quartz and its Rayleigh line. The state of the Al is then determined as the intersection point of the Al Hugoniot and the release curve of the Al, which crosses the state of the quartz. Finally, the state of the BN is determined by the intersection of the release curve of Al and the Rayleigh line of BN. In our analysis, we used the approximation that the release curve is the mirror curve of the Hugoniot in the u_p–P plane with respect to the intersection point. Although our shocks are not weak, we checked that the differences between the real release curve of Al and the mirror Hugoniot curves

23 September 2024 06:07:34

© Author(s) 2024

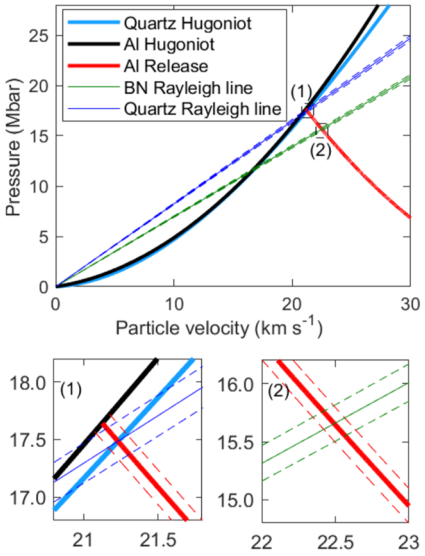

FIG. 5. IM analysis in the pressure vs particle velocity plane for a typical shot using the Al–BN–quartz target (shot 046). The state of the quartz in this shot is determined by the intersection of the Hugoniot curve with the measured quartz Rayleigh line [plot (1)]. The Al release line going through this point is then determined. The intersections with the standard Al Hugoniot and the measured BN Rayleigh line determine the states of Al and BN along the respective Hugoniot [plot (2)]. Uncertainty ranges are shown by the dashed lines. The main source of errors in the IM analysis comes from the shock velocity measurements.

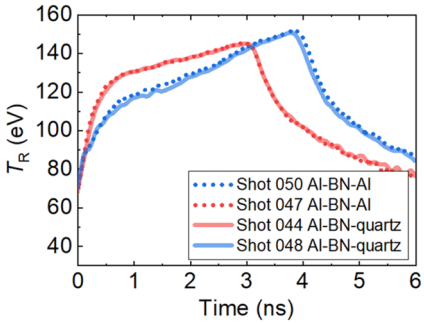

FIG. 6. Time-resolved X-ray radiation temperatures measured in the shots, illustrating the reproducibility of the X-ray drive. The unsteady-shock corrections calculated for the Al–BN–quartz shots 044 and 048 (solid lines) can be used in the Al–BN–Al shots 047 and 050 (dotted lines), respectively.

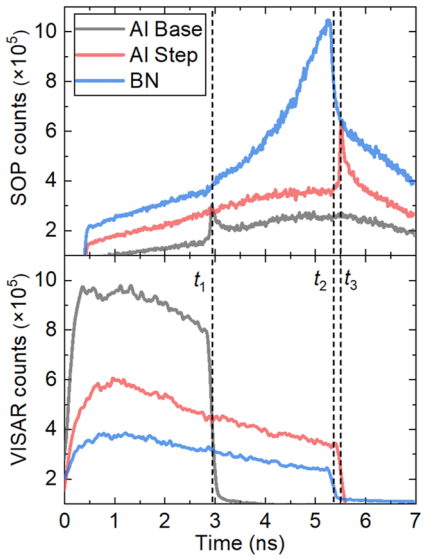

FIG. 7. Data analysis for the Al–BN–Al target in shot 047. The time-resolved VISAR and SOP counts in the Al base, BN, and Al are plotted. t_1, t_2, and t_3 are the shock breakout times from the Al base, the BN, and the Al step, respectively. These times were determined as the half-height positions of the corresponding rising/dropping slopes. The shock transit times in the BN and Al step were calculated as $\Delta t_{BN} = t_2 - t_1$ and $\Delta t_{Al} = t_3 - t_1$.

are negligible in our pressure range and become significant only at much lower pressures. The 1σ variations were also considered and are drawn in Fig. 5 around the release curves and the Rayleigh lines. These variations determine the measurement errors for the shocked state of BN.

To reduce possible systematic errors from using Al–BN–quartz targets, in which the shock velocity in the Al base was not directly measured, the Al–BN–Al targets were shocked under the same radiation sources. Time-resolved X-ray radiation temperatures recorded by FXRDs are shown in Fig. 6. The radiation temperatures measured with Al–BN–Al targets (solid lines) and Al–BN–quartz targets (dotted lines) were indeed very close. The maximum deviation of 2% in temperature profiles was within the ~3% diagnostic uncertainty. Therefore, the quartz shock velocity history measured in the Al–BN–quartz sample can be used as the basis for correcting the nonstationary effects in the Al–BN–Al samples. The high reproducibility of the radiation temperatures ensures the reliability of the analysis.

Figure 7 illustrates shock-breakout signals extracted from the raw data for Al–BN–Al targets. The shock breakout times from the Al base, from the BN sample, and from the Al step were measured from the same image. Only the Al standard was used as reference material in the IM analysis described in previous works.[33,55] The average shock velocity in the Al step, U_S^{Al}, was measured directly from the thickness of the step and the shock transit time. It was then corrected using the measured quartz shock velocity history in the Al–BN–quartz target by the inherent time modulation factor F_{BN-Al}. To be specific, shock velocities in Al for shots 047 and 050 were corrected by using shots 044 and 048 in quartz, respectively. In this work, the F_{BN-Al} factor for BN with Al reference was calculated to be ~0.99, too.

The measured shock Hugoniot data in the two types of targets are listed in Tables I and II, respectively. In these experiments, h-BN samples with initial densities of 2.04 g/cm^3 and 2.05 g/cm^3 were compressed to a shocked density of 5.00–6.05 g/cm^3, corresponding to compression ratios of ~2.5 to 3. The Hugoniot data obtained by two different IM routes show good consistency, adding confidence in the reliability of the experimental results. The uncertainty of the shock velocity in Al is less than 1%, while the maximum uncertainty

23 September 2024 06:07:34

© Author(s) 2024

TABLE I. Shock Hugoniot data obtained from the Al–BN–quartz targets. U_S^Q and U_S^{BN} are the measured shock velocities of quartz and BN, respectively. The particle velocity u_p^{Al} was calculated using the IM between the Al and quartz standards. The particle velocity u_P^{BN}, pressure P^{BN}, and compression ratio ρ^{BN}/ρ_0^{BN} for shocked BN were determined by IM between the BN and Al. The uncertainties calculated by propagating the errors in the shock velocities are also shown.

Shot	U_S^Q (km/s)	U_S^{BN} (km/s)	u_P^{Al} (km/s)	u_P^{BN} (km/s)	P^{BN} (Mbar)	ρ^{BN}/ρ_0^{BN}
043	23.91 ± 0.54	25.69 ± 0.22	14.91 ± 0.45	16.03 ± 0.22	8.35 ± 0.29	2.66 ± 0.18
044	22.87 ± 0.36	24.45 ± 0.22	14.02 ± 0.31	15.01 ± 0.43	7.53 ± 0.22	2.61 ± 0.13
046	31.27 ± 0.79	34.12 ± 0.32	21.22 ± 0.67	22.61 ± 0.95	15.74 ± 0.67	2.97 ± 0.25
048	20.04 ± 0.27	21.38 ± 0.63	11.60 ± 0.31	12.49 ± 0.35	5.47 ± 0.18	2.40 ± 0.16
051	19.70 ± 0.26	20.70 ± 0.16	11.30 ± 0.22	12.25 ± 0.31	5.17 ± 0.13	2.45 ± 0.10

TABLE II. Shock Hugoniot data obtained from the Al–BN–Al target. U_S^{Al} and U_S^{BN} are the shock velocities measured in Al and BN. The particle velocity for Al, u_p^{Al}, was calculated from the Al Hugoniot. The particle velocity u_P^{BN}, pressure P^{BN}, and compression ratio ρ^{BN}/ρ_0^{BN} for shocked BN were determined by IM between BN and Al. The uncertainties calculated by propagating the errors in the shock velocities are also shown.

Shot	U_S^{Al} (km/s)	U_S^{BN} (km/s)	u_P^{Al} (km/s)	u_P^{BN} (km/s)	P^{BN} (Mbar)	ρ^{BN}/ρ_0^{BN}
047	24.18 ± 0.14	25.87 ± 0.19	15.14 ± 0.12	16.30 ± 0.23	8.60 ± 0.12	2.70 ± 0.08
050	21.84 ± 0.15	23.16 ± 0.19	13.14 ± 0.13	14.19 ± 0.21	6.71 ± 0.10	2.58 ± 0.07

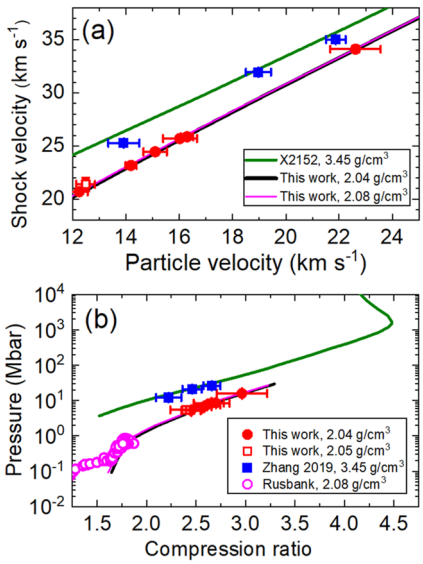

FIG. 8. Comparisons of theoretical BN Hugoniots with shock experiments. The data are presented in (a) the U_s–u_p plane and (b) the pressure–compression plane. For the theoretical curves, our DFT-MD Hugoniots for h-BN were calculated for the initial density 2.04 g/cm^3 (solid black) and the initial density 2.08 g/cm^3 (solid purple). The Hugoniot for c-BN (solid green) from Zhang *et al.*[23] was calculated starting from ρ_0 = 3.45 g/cm^3 with model X2152. The experimental data for h-BN obtained in this study are shown in red. Our measurements and DFT-MD simulations are highly consistent up to 16 Mbar. As a comparison, the shock Hugoniot data for c-BN from previous experiments[23] and for h-BN from RUSBANK[15,16] are also shown.

of the shock velocity in BN is 2.2%. In Table I, the greatest uncertainty in the shock velocity for BN corresponds to shot 048. This is due to the large surface roughness in BN samples, as shown in Tables S3 and S4 (supplementary material). Figure 8 presents experimental and theoretical Hugoniot curves of BN for three different initial densities: the results from Zhang *et al.*,[23] the RUSBANK data,[16] and our data. These correspond to 3.45, 2.08, and 2.04 g/cm^3 initial densities, respectively.

Figure 8 compares the theoretical and experimental BN Hugoniot data under shock compression. The measured Hugoniot data in this work are highly consistent with our DFT-MD simulations for 2.04 g/cm^3. In the pressure–compression ratio relation, our experimental results and DFT-MD calculations also agree well. Our experimental results provide a strong constraint on theoretical models of the BN EoS up to 16 Mbar.

V. CONCLUSIONS

In the experiments described here, high-pressure data for the shock Hugoniot of h-BN were for the first time obtained in the range 5–16 Mbar using the SGIII-p laser facility. These data complement the existing datasets for h-BN at low pressure (from RUSBANK) and c-BN at high pressure (from OMEGA experiments), filling a gap in present knowledge of the properties of boron and its compounds at extreme pressures. In parallel to the experiments, our DFT-MD calculations provide results that are in very good agreement with available Hugoniot data. This gives confidence in the validity of DFT-MD results under conditions of extremely high pressures and

23 September 2024 06:07:34

© Author(s) 2024

temperatures. The melting temperature of h-BN along the principal Hugoniot in the calculations is almost a factor of two below the melting temperature of diamond along its Hugoniot.[58] Thus, detecting high-pressure melting for BN and determining the melting curves under laser shock compression experiments in the future work is an important task with regard to exploring the possibility of using boron compound materials as ablators in inertial confinement experiments to improve implosion performance. From the point of view of materials science, our calculations imply a phase transition from h-BN to c-BN at a pressure of ~0.1 Mbar. It will also be interesting to extend the DFT-MD calculations at relatively low temperature to investigate the presence of other high-pressure phases and perform experiments in this range with newly developed *in situ* X-ray diffraction techniques at high-power laser or X-ray free-electron laser facilities in the near future.[59] Our results provide fundamental scientific insight into the structural complexity of the BN phase plane under extreme conditions, which is of interest for inertial confinement fusion, hydrogen–boron fusion, and high-energy-density physics.

SUPPLEMENTARY MATERIAL

The supplementary material provides details of the targets and samples, the unsteady correction and *F* factor, and the uncertainties in sample thickness.

ACKNOWLEDGMENTS

We thank Ji Yan, Lifeng Wang, and Weichao Tong for helpful discussions. We acknowledge the crucial contributions from the SGIII-Prototype laser management, staff, and support team for shots and from the target fabrication team for providing the targets. This work is supported by the National Natural Science Foundation of China under Grant No. 12035002. D.B. is a Visiting Professor at Peking University.

AUTHOR DECLARATIONS

Conflict of Interest

The authors have no conflicts to disclose.

Author Contributions

H.Z. and Y.Y. contributed equally to this work.

W.K., L.S., and D.B. conceived the work; H.Z., L.S., Z.-Y.G., W.-M.Y., Y.-G.L., S.-W.L., H.L., X.-X.D., Z.-B.W., D.Y., J.-M.Y., and D.B. performed the experiments; M.-S.Y. prepared the samples; Y.-T.Y., J.-X.S., and W.K. performed calculations; H.Z., K.B., and D.S. analyzed the data with assistance from D.B. and Z.-B.W.; K.B., K.L., Y.-S.L., W.-Y.H., J.-M.Y., Z.-Q.Z, and W.-Y.Z. contributed to the interpretation of the data; and Z.H. and Y.-T.Y. wrote the paper. All coauthors commented critically on the manuscript.

Huan Zhang: Investigation (equal); Writing – original draft (equal). **Yutong Yang**: Investigation (equal); Writing – original draft (equal). **Weimin Yang**: Investigation (supporting). **Zanyang Guan**: Investigation (supporting). **Xiaoxi Duan**: Data curation (equal); Investigation (equal). **Mengsheng Yang**: Data curation (equal); Investigation (supporting). **Yonggang Liu**: Data curation (supporting); Investigation (supporting). **Jingxiang Shen**: Investigation (supporting). **Katarzyna Batani**: Data curation (supporting); Formal analysis (supporting); Investigation (supporting). **Diluka Singappuli**: Data curation (equal). **Ke Lan**: Investigation (supporting); Writing – review & editing (supporting). **Yongsheng Li**: Data curation (supporting); Investigation (supporting). **Wenyi Huo**: Conceptualization (supporting); Data curation (supporting); Investigation (supporting). **Hao Liu**: Conceptualization (supporting); Investigation (supporting). **Yulong Li**: Conceptualization (supporting); Investigation (supporting). **Dong Yang**: Investigation (supporting). **Sanwei Li**: Formal analysis (supporting); Validation (supporting). **Zhebin Wang**: Investigation (supporting). **Jiamin Yang**: Formal analysis (supporting); Investigation (supporting). **Zongqing Zhao**: Formal analysis (supporting); Investigation (supporting); Project administration (supporting). **Weiyan Zhang**: Investigation (supporting); Project administration (supporting); Supervision (supporting). **Liang Sun**: Conceptualization (equal); Investigation (equal); Writing – review & editing (equal). **Wei Kang**: Conceptualization (equal); Investigation (equal); Writing – review & editing (equal). **Dimitri Batani**: Conceptualization (equal); Investigation (equal); Writing – original draft (equal); Writing – review & editing (equal).

DATA AVAILABILITY

The source data are provided and shown in the figures and tables. Additional data are available from the corresponding author upon request.

REFERENCES

[1] D. K. Duncan, F. Primas, L. M. Rebull, A. M. Boesgaard, C. P. Deliyannis *et al.*, "The evolution of galactic boron and the production site of the light elements," Astrophys. J. **488**, 338 (1997).

[2] J. J. Cowan, C. Sneden, J. E. Lawler, A. Aprahamian, M. Wiescher *et al.*, "Origin of the heaviest elements: The rapid neutron-capture process," Rev. Mod. Phys. **93**, 015002 (2021).

[3] A. M. Boesgaard, "The light elements lithium, beryllium and boron," in Origin and Evolution of the Elements, edited by A. McWilliam and M. Rauch (Cambridge University Press, Cambridge, 2004), pp. 117.

[4] M. Gatu Johnson, D. T. Casey, M. Hohenberger, A. B. Zylstra, A. Bacher *et al.*, "Optimization of a high-yield, low-areal-density fusion product source at the National Ignition Facility with applications in nucleosynthesis experiments," Phys. Plasmas **25**, 056303 (2018).

[5] M. Gatu Johnson, A. B. Zylstra, A. Bacher, C. R. Brune, D. T. Casey *et al.*, "Development of an inertial confinement fusion platform to study charged-particle-producing nuclear reactions relevant to nuclear astrophysics," Phys. Plasmas **24**, 041407 (2017).

[6] D. Batani, D. Margarone, and F. Belloni, "Advances in the study of laser-driven proton–boron fusion," Laser Part. Beams **2023**, e5, part of Special Issue: For an extended presentation of recent developments in proton–boron fusion research.

[7] M.-S. Liu, H.-S. Xie, Y.-M. Wang, J.-Q. Dong, K.-M. Feng *et al.*, "ENN's roadmap for proton-boron fusion based on spherical torus," Phys. Plasmas **31**, 062507 (2024).

[8] R. M. Magee, K. Ogawa, T. Tajima, I. Allfrey, H. Gota *et al.*, "First measurements of $p^{11}B$ fusion in a magnetically confined plasma," Nat. Commun. **14**, 955 (2023).

[9] K. Batani, D. Batani, X. T. He, and K. Shigemori, "Recent progress in matter in extreme states created by laser," Matter Radiat. Extremes **7**, 013001 (2021), part of

23 September 2024 06:07:34

© Author(s) 2024

Special Issue: For an extended presentation of recent developments in research on matter under extreme conditions, see the special issue of Matter and Radiation at Extremes.
[10]H.-K. Mao, B. Chen, H. Gou, K. Li, J. Liu, *et al.*, "2022 HP special volume: Interdisciplinary high pressure science and technology," Matter Radiat. Extremes **8**, 063001 (2023).
[11]H.-K. Mao, "Hydrogen and related matter in the pressure dimension," Matter Radiat. Extremes **7**, 063001 (2022).
[12]E. Knittle, R. M. Wentzcovitch, R. Jeanloz, and M. L. Cohen, "Experimental and theoretical equation of state of cubic boron nitride," Nature **337**, 349–352 (1989).
[13]A. F. Goncharov, J. C. Crowhurst, J. K. Dewhurst, S. Sharma, C. Sanloup *et al.*, "Thermal equation of state of cubic boron nitride: Implications for a high-temperature pressure scale," Phys. Rev. B **75**, 224114 (2007).
[14]V. L. Solozhenko, D. Häusermann, M. Mezouar, and M. Kunz, "Equation of state of wurtzitic boron nitride to 66 GPa," Appl. Phys. Lett. **72**, 1691–1693 (1998).
[15]See http://www.ihed.ras.ru/RUSBANK/.
[16]S. P. Marsh, LASL Shock Hugoniot Data (University of California Press, 1980).
[17]H. Zhang, D. Kang, C. Wu, L. Hao, H. Shen *et al.*, "Semi-hydro-equivalent design and performance extrapolation between 100 kJ-scale and NIF-scale indirect drive implosion," Matter Radiat. Extremes **9**, 015601 (2023).
[18]Y.-H. Chen, Z. Li, H. Cao, K. Pan, S. Li *et al.*, "Determination of laser entrance hole size for ignition-scale octahedral spherical hohlraums," Matter Radiat. Extremes **7**, 065901 (2022).
[19]A. Tentori, A. Colaïtis, and D. Batani, "3D Monte-Carlo model to study the transport of hot electrons in the context of inertial confinement fusion. Part I," Matter Radiat. Extremes **7**, 065902 (2022).
[20]H. D. Whitley, G. E. Kemp, C. B. Yeamans, Z. B. Walters, B. E. Blue *et al.*, "Comparison of ablators for the polar direct drive exploding pusher platform," High Energy Density Phys. **38**, 100928 (2021).
[21]A. C. Hayes-Sterbenz, G. M. Hale, G. Jungman, and M. W. Paris, Probing the Physics of Burning DT Capsules Using Gamma-Ray Diagnostics (Los Alamos National Lab (LANL), Los Alamos, NM, 2015).
[22]H. Abu-Shawareb *et al.*, "Lawson criterion for ignition exceeded in an inertial fusion experiment," Phys. Rev. Lett. **129**, 075001 (2022).
[23]S. Zhang, A. Lazicki, B. Militzer, L. H. Yang, K. Caspersen *et al.*, "Equation of state of boron nitride combining computation, modeling, and experiment," Phys. Rev. B **99**, 165103 (2019).
[24]S. Zhang, B. Militzer, M. C. Gregor, K. Caspersen, L. H. Yang *et al.*, "Theoretical and experimental investigation of the equation of state of boron plasmas," Phys. Rev. E **98**, 023205 (2018).
[25]D. E. Fratanduono, P. M. Celliers, D. G. Braun, P. A. Sterne, S. Hamel *et al.*, "Equation of state, adiabatic sound speed, and Gruneisen coefficient of boron carbide along the principal Hugoniot to 700 GPa," Phys. Rev. B **94**, 184107 (2016).
[26]S. Zhang, M. C. Marshall, L. H. Yang, P. A. Sterne, B. Militzer *et al.*, "Benchmarking boron carbide equation of state using computation and experiment," Phys. Rev. E **102**, 053203 (2020).
[27]B. Wilson, V. Sonnad, P. Sterne, and W. Isaacs, "Purgatorio—A new implementation of the Inferno algorithm," J. Quant. Spectrosc. Radiat. Transfer **99**, 658–679 (2006).
[28]T. Gong, L. Hao, Z. Li, D. Yang, S. Li *et al.*, "Recent research progress of laser plasma interactions in Shenguang laser facilities," Matter Radiat. Extremes **4**, 055202 (2019).
[29]K. Lan, "Dream fusion in octahedral spherical hohlraum," Matter Radiat. Extremes **7**, 055701 (2022).
[30]Z. Li, X. Jiang, S. Liu, T. Huang, J. Zheng *et al.*, "A novel flat-response x-ray detector in the photon energy range of 0.1–4 keV," Rev. Sci. Instrum. **81**, 073504 (2010).
[31]Z. Li, X. Zhu, X. Jiang, S. Liu, J. Zheng *et al.*, "Note: Continuing improvements on the novel flat-response x-ray detector," Rev. Sci. Instrum. **82**, 106106 (2011).
[32]W. Liu, X. Duan, S. Jiang, Z. Wang, L. Sun *et al.*, "Laser-driven shock compression of gold foam in the terapascal pressure range," Phys. Plasmas **25**, 062707 (2018).
[33]P. Wang, C. Zhang, S. Jiang, X. Duan, H. Zhang *et al.*, "Density-dependent shock Hugoniot of polycrystalline diamond at pressures relevant to ICF," Matter Radiat. Extremes **6**, 035902 (2021).
[34]D. E. Fratanduono, D. H. Munro, P. M. Celliers, and G. W. Collins, "Hugoniot experiments with unsteady waves," J. Appl. Phys. **116**, 033517 (2014).
[35]P. M. Celliers and M. Millot, "Imaging velocity interferometer system for any reflector (VISAR) diagnostics for high energy density sciences," Rev. Sci. Instrum. **94**, 011101 (2023).
[36]J. D. Kilkenny, M. D. Cable, C. A. Clower, B. A. Hammel, V. P. Karpenko *et al.*, "Diagnostic systems for the national ignition facility (NIF) (invited)," Rev. Sci. Instrum. **66**, 288–295 (1995).
[37]F. Wang, S. Jiang, Y. Ding, S. Liu, J. Yang *et al.*, "Recent diagnostic developments at the 100 kJ-level laser facility in China," Matter Radiat. Extremes **5**, 035201 (2020).
[38]J. E. Miller, T. R. Boehly, A. Melchior, D. D. Meyerhofer, P. M. Celliers *et al.*, "Streaked optical pyrometer system for laser-driven shock-wave experiments on OMEGA," Rev. Sci. Instrum. **78**, 034903 (2007).
[39]D. G. Hicks, T. R. Boehly, P. M. Celliers, J. H. Eggert, E. Vianello *et al.*, "Shock compression of quartz in the high-pressure fluid regime," Phys. Plasmas **12**, 082702 (2005).
[40]W. Kohn and L. J. Sham, "Self-consistent equations including exchange and correlation effects," Phys. Rev. **140**, A1133–A1138 (1965).
[41]P. Hohenberg and W. Kohn, "Inhomogeneous electron gas," Phys. Rev. **136**, B864–B871 (1964).
[42]N. de Koker, "Melting of cubic boron nitride at extreme pressures," J. Phys.: Condens.Matter **24**, 055401 (2012).
[43]F. R. Corrigan and F. P. Bundy, "Direct transitions among the allotropic forms of boron nitride at high pressures and temperatures," J. Chem. Phys. **63**, 3812–3820 (1975).
[44]V. L. Solozhenko, "Boron nitride phase diagram. State of the art," High Pressure Res. **13**, 199–214 (1995).
[45]P. Giannozzi, S. Baroni, N. Bonini, M. Calandra, R. Car *et al.*, "QUANTUM ESPRESSO: A modular and open-source software project for quantum simulations of materials," J. Phys, Condens. Matter **21**, 395502 (2009).
[46]J. P. Perdew and Y. Wang, "Accurate and simple analytic representation of the electron-gas correlation energy," Phys. Rev. B **45**, 13244–13249 (1992).
[47]N. A. W. Holzwarth, A. R. Tackett, and G. E. Matthews, "A projector augmented wave (PAW) code for electronic structure calculations, Part I: Atompaw for generating atom-centered functions," Comput. Phys. Commun. **135**, 329–347 (2001).
[48]P. E. Blöchl, "Projector augmented-wave method," Phys. Rev. B **50**, 17953–17979 (1994).
[49]S. Zhang, H. Wang, W. Kang, P. Zhang, and X. T. He, "Extended application of Kohn–Sham first-principles molecular dynamics method with plane wave approximation at high energy—From cold materials to hot dense plasmas," Phys. Plasmas **23**, 042707 (2016).
[50]C. Gao, S. Zhang, W. Kang, C. Wang, P. Zhang, and X. T. He, "Validity boundary of orbital-free molecular dynamics method corresponding to thermal ionization of shell structure," Phys. Rev. B **94**, 205115 (2016).
[51]X. Liu, X. Zhang, C. Gao, S. Zhang, C. Wang *et al.*, "Equations of state of poly-α-methylstyrene and polystyrene: First-principles calculations versus precision measurements," Phys. Rev. B **103**, 174111 (2021).
[52]C. Gao, X. Liu, S. Zhang, W. Kang, P. Zhang, and X. T. He, "Consistent wide-range equation of state of silicon by a unified first-principles method," Phys. Rev. B **107**, 165150 (2023).
[53]D. Kang, Y. Hou, Q. Zeng, and J. Dai, "Unified first-principles equations of state of deuterium-tritium mixtures in the global inertial confinement fusion region," Matter Radiat. Extremes **5**, 055401 (2020).
[54]H. Y. Sun, D. Kang, Y. Hou, and J. Y. Dai, "Transport properties of warm and hot dense iron from orbital free and corrected Yukawa potential molecular dynamics," Matter Radiat. Extremes **2**, 287–295 (2017).

23 September 2024 06:07:34

© Author(s) 2024

[55]X. Duan, Z. Wang, C. Zhang, L. Sun, Q. Ye *et al.*, "A method for impedance-match experiments with unsteady shock loading," (unpublished) (2024).
[56]P. M. Celliers, G. W. Collins, D. G. Hicks, and J. H. Eggert, "Systematic uncertainties in shock-wave impedance-match analysis and the high-pressure equation of state of Al," J. Appl. Phys. **98**, 113529 (2005).
[57]S. Hamel, L. X. Benedict, P. M. Celliers, M. A. Barrios, T. R. Boehly *et al.*, "Equation of state of $CH_{1.36}$: First-principles molecular dynamics simulations and shock-and-release wave speed measurements," Phys. Rev. B **86**, 094113 (2012).
[58]J. H. Eggert, D. G. Hicks, P. M. Celliers, D. K. Bradley, R. S. McWilliams *et al.*, Nat. Phys. **6**, 40–43 (2010).
[59]S. Makarov, S. Dyachkov, T. Pikuz, K. Katagiri, H. Nakamura *et al.*, "Direct imaging of shock wave splitting in diamond at Mbar pressure," Matter Radiat. Extremes **8**, 066601 (2023).

23 September 2024 06:07:34

© Author(s) 2024